Delamination of a rigid punch from an elastic substrate under normal and shear forces

XiaoHao Sun[1,2], Luxia Yu[2], Mark Rentschler[2], HengAn Wu[1*], Rong Long[2*]

[1]CAS Key Laboratory of Mechanical Behavior and Design of Materials, Department of Modern Mechanics, CAS Center for Excellence in Complex System Mechanics, University of Science and Technology of China, Hefei, Anhui 230027, China.

[2]Department of Mechanical Engineering, University of Colorado Boulder, Boulder, CO 80309, USA.

*Correspondence should be addressed to R. Long (rong.long@colorado.edu) or H.A. Wu (wuha@ustc.edu.cn)

Abstract

Delamination of rigid objects from an elastic substrate with finite thickness is a fundamental problem underlying applications such as marine fouling release coatings or anti-icing coatings. Most existing theoretical studies assume that delamination is driven by forces normal to the substrate surface, while in practice the delamination force may also include shear components that are parallel to the substrate surface. In this work, we consider a model system where a rigid cylindrical punch is detached from an elastic substrate under normal force, shear force or both. Our focus is to determine the pull-off force and to reveal the delamination mechanics under various geometrical and loading conditions, specifically the substrate thickness and the position and angle of the delamination force. To gain theoretical insights, we first study a plane strain model where a long rigid strip is adhered to an elastic half-space, and obtain an analytical solution revealing how the pull-off force depends on the loading position and angle. Moreover, we develop a three-dimensional finite element model to simulate the delamination of a rigid cylindrical punch from an elastic substrate with finite thickness. Three delamination modes are identified from finite element results: Mode-I crack propagation, Mode-II crack propagation, and interface cavitation. For the first two modes, we obtain empirical formulas to calculate the pull-off force using adhesion energy, substrate modulus, contact radius and substrate thickness. We also find that the analytical solution derived from the plan strain model can serve as a qualitative guide to estimate the effect of loading position and angle on the pull-off force.

Keywords

Adhesion, delamination, pull-off force, interface fracture, finite element simulations.

1. Introduction

Adhesion of rigid objects on elastomeric coatings is a ubiquitous problem found in many engineering applications. For example, marine biofouling, caused by the undesirable attachment of marine organisms to submerged surfaces such as ship hulls, can increase the weight of marine vessels and roughen the hull surface, leading to reduced fuel efficiency[1] and increased maintenance costs[2]. Conventional antifouling coatings are mainly based on using broad spectrum biocides to prevent the settlement and growth of marine organisms[3,4]. Serious environment concerns have been raised towards such toxic coatings[4,5], and new non-toxic technologies to address the biofouling problem are highly desirable[6–9]. One approach is to implement fouling release coatings (FRCs)[6] consisting of polydimethylsiloxane (PDMS) or other soft elastomers[10]. Instead of preventing the attachment of fouling organisms, FRCs can promote release of the already attached fouling organisms under external forces[6] due to their low surface energy and compliance. Low adhesion strength is also desired for deicing or anti-icing applications, i.e., to mitigate the hazardous ice accretion on aircrafts or wind turbines. Icephobic coatings based on soft elastomers[11–14] have been recently developed to reduce the force required to release ice blocks from the coating surface.

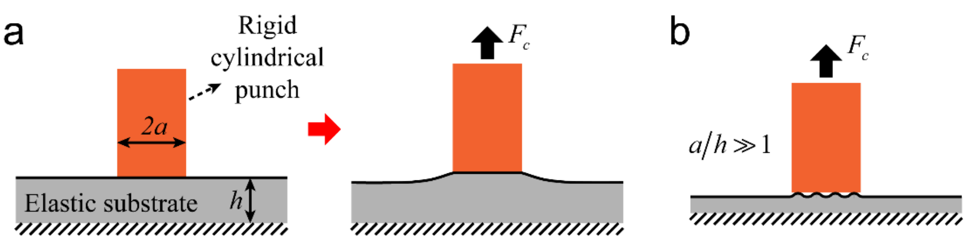

Figure 1 (a) Delamination of a rigid cylindrical punch from an elastic substrate under normal force. (b) Interface cavitation may occur in the limit of thin substrate (a/h >>1).

In both applications described above, the force required to delaminate a rigid object, either a barnacle or an ice block, adhered to the coating surface is an important metric for evaluating effectiveness of the coating. Theoretical modeling of the adhesion mechanics involved in the delamination process can enable the prediction of adhesive forces, and thus is an important step for designing FRCs or icephobic coatings. The most widely used model consists of a rigid cylindrical punch, which represents the fouling organism (e.g. barnacle) or ice block, in adhesive contact with a soft elastic substrate (i.e., the coating layer) bonded to a rigid backing surface (see Fig.1a). This model was analyzed in a pioneering work by Kendall[15] where delamination was assumed to be driven by a force normal to the substrate. Using an energy approach, Kendall[15] derived the force required to detach the punch from the substrate, referred to as the pull-off force F_c, in two limiting cases. When the substrate (thickness: h) is thick in comparison to the punch radius a, the pull-off force is

$$F_c = \pi a^2 \sqrt{\frac{8EW_{ad}}{\pi a\left(1-\nu^2\right)}}, \qquad (h >> a), \tag{1.1}$$

where E and ν are the Young's modulus and Poisson's ratio of the substrate, respectively, and W_{ad} is the work of adhesion, i.e. the energy per unit area needed to separate the punch from the substrate. On the other hand, the thin substrate limit, namely $h << a$, is more useful in practice since most coatings fall into the limit. According to Kendall[15], the pull-off force in the thin substrate limit is

$$F_c = \pi a^2 \sqrt{\frac{2KW_{ad}}{h}} = \pi a^2 \sqrt{\frac{2EW_{ad}}{3\left(1-2\nu\right)h}}, \quad (h << a), \tag{1.2}$$

where K is the bulk modulus. However, elastomers are typically incompressible, i.e., ν close to 1/2 and K approaching infinity, for which Eq.(1.2) would predict an infinite pull-off force and thus is not valid. To understand the origin of this limitation, we note that Eq.(1.2) was based on the following result for the substrate compliance C proposed by Kendall[15]:

$$C = \frac{\Delta}{F} = \frac{h}{\pi a^2 K} \qquad (h << a), \tag{1.3}$$

where F is the force applied to the punch and Δ is the corresponding displacement. Note that for a flat punch with a fixed contact area and assuming linear elasticity, the mechanical response of the substrate is linear, i.e., Δ is proportional to F. When the substrate is incompressible, Eq.(1.3) implies that the substrate compliance is zero, which further leads to the singular pull-off force in Eq.(1.2). Physically this is because when the thin substrate is confined between two rigid surfaces (i.e., punch and backing surface), the incompressibility constraint can prevent deformation of the substrate and thus diminish the compliance. This phenomenon was studied by Lin et al.[16] in detail, where the compliance of thin substrate ($h << a$) was found to be similar to Eq.(1.3) except an additional correction factor $(1+\nu)/[3(1-\nu)]$. This correction factor is equal to 1 when ν=1/2.

The theoretical difficulty invoked by the bulk modulus in Eq.(1.2) was addressed by Yang and Li[17] who performed a rigorous analysis for incompressible substrate (ν = 1/2) with finite thickness. Specifically, they considered two different types of frictional boundary conditions, no-slip or frictionless, at two interfaces: i) between the punch and the substrate, ii) between the substrate and the backing surface. If the no-slip condition was assumed on both interfaces, the compliance C in the thin substrate limit was found to be[17]

$$C = \frac{2h^3}{\pi a^4 E} \qquad (h << a). \qquad (1.4)$$

In comparison to Eq.(1.3), the unbounded bulk modulus K is replaced by the Young's modulus E in Eq.(1.4). The low compliance due to the confinement of thin substrates is reflected in the higher-order dependence of C on h/a (i.e., $C \sim h^3/a^3$ instead of $\sim h/a$ as $h/a \to 0$). The pull-off force corresponding to Eq.(1.4) was found to be[17]

$$F_c = \pi a^2 \sqrt{\frac{EW_{ad}}{2h}\frac{a}{h}}, \qquad (h << a). \qquad (1.5)$$

This solution predicts that F_c scales with the coating thickness h as $F_c \sim h^{-3/2}$, while Kendall's theory predicts that $F_c \sim h^{-1/2}$. Interestingly, the latter scaling, i.e., $F_c \sim h^{-1/2}$, was often observed in experimental data with thin substrates, e.g., in adhesion experiments between plastic discs and gelatin thin films[15] and between epoxy studs and silicone elastomer coatings[18,19], despite the theoretical rigorousness of the solution in Eq.(1.5). Yang and Li[17] showed that if the frictionless condition is assumed on both interfaces, the pull-off force is $F_c = \pi a^2 \sqrt{8EW_{ad}/3h}$, much smaller than that in Eq.(1.5) since a/h>>1. This is because the frictionless interfaces allow lateral strain in the substrate and thus can relax the confinement effect. Although the scaling $F_c \sim h^{-1/2}$ for frictionless interfaces is consistent with experimental observations, in practice the coating layer is typically well bonded to the backing surface[20] where the no-slip condition should prevail. Indeed, in this work we assume the elastic substrate is bonded perfectly to the rigid backing surface (see Fig.1a). On the punch/substrate interface, we assume strong friction and model it using a mixed-mode fracture criterion.

The discrepancy outlined above was reconciled by Chung and Chaudhury[21] who pointed out that for very thin incompressible substrates ($h << a$), the delamination process does not initiate at the periphery of the punch, followed by an unstable interface crack propagation inward, as assumed by Kendall[15] and Yang and Li[17]. Instead, delamination initiates due to the interface cavitation instability (see Fig.1b)[21–26]. Interface cavitation allows local delamination within the contact area and can also relax the confinement effect for thin and incompressible substrates. In this case, the pull-off force was determined through a perturbation analysis[21]:

$$F_c = \pi a^2 \sqrt{\frac{3.3 W_{ad} E}{h}}, \qquad (h << a), \tag{1.6}$$

which gives a scaling relation $F_c \sim h^{-1/2}$ consistent with experimental observations. Furthermore, experimental verification of the scaling relation $F_c \sim (W_{ad}E/h)^{1/2}$ was reported in Chaudhury et al.[27] who used a well-defined model system to control E and W_{ad} independently and to observe interface cavitation *in situ*.

All studies reviewed above are based on the assumption that the delamination force is normal to the coating surface. In reality, the delamination force can come from different physical origins depending on the applications. For example, the force to release barnacles or other fouling organisms from a FRC can be provided by the hydrodynamic shear forces for a cruising ship[28], and the force for ice release can come from the aerodynamic shear force for an aircraft or the centripetal force for a rotating wind turbine. In all of these scenarios, the delamination force may include components both parallel and normal to the coating surface[29,30]. In particular, the adhesion strength of ice on icephobic coatings is often tested under the shear mode and reported as the average shear stress at pull-off τ_{ice}, i.e., the pull-off force divided by the contact area[12–14]. Although many theoretical[15–17,21,26,31–33] and experimental works[21,23–26] have been performed on the delamination mechanics under normal forces, much less work[20] has been done for the mechanics of delamination under shear forces or combined normal and shear forces. The brief review above implies that even under normal delamination, the pull-off force is sensitive to the interface separation process. If shear force is present, the stress state of the substrate during delamination becomes inherently three-dimensional (3D), and a systematic understanding on how such 3D stress state affects the interface separation process is currently lacking.

The focus of this paper is on the delamination mechanics involving a rigid cylindrical punch in adhesive contact with an elastic substrate under normal and shear forces. This model system is widely used to evaluate the performance of elastomeric fouling release and icephobic coatings. The delamination of a cylindrical punch under shear forces involves 3D stress/strain states in the substrate. To gain theoretical insights towards this complex problem, we first consider a plane strain geometry in Section 2 where a rigid rectangular punch is detached from an elastic half-space (with infinite thickness), and obtain analytical solutions for the pull-off force under combined shear and normal forces. In Sections 3 and 4, we study the delamination of a rigid cylindrical punch from an elastic substrate with finite thickness using a 3D finite element (FE) model. The model is described in Section 3 while the results are presented and discussed in Section 4. Specifically, we identify the pull-off force for different substrate thickness and loading modes, based on which empirical formulas are developed. The various delamination modes revealed by the FE results and how they are related to the pull-off forces are also discussed. Conclusions are given in Section 5.

2. Plane strain model: 2D analytical solution

2.1 Problem description

In this section, we consider the delamination of a long rigid punch from an elastic half-space as shown in Fig.2a. To facilitate analysis, a Cartesian coordinate system is introduced such that the *x*-*y* plane coincides with the surface of the half-space and the *z*-axis is directed into the half-space. The punch, assumed to be infinitely long along the *y*-axis, is in adhesive contact with the half-space and is under line forces P and Q (unit: N/m and distributed along the y-axis) that are normal and parallel to the x-y plane, respectively. The delamination process can be modeled as a two-dimensional (2D) plane strain problem in the x-z plane, as shown in Fig.2b. The origin O is located at the midpoint of the contact area which occupies the region from $x = -a$ to $x = a$.

We assume the half-space to be a linear elastic solid with Young's modulus E and Poisson's ratio $\nu=0.5$. The latter is motivated by the fact that most of the soft fouling release or anti-icing coatings consist of silicone elastomers (e.g. PDMS) which are incompressible[6,14,34]. In addition, experimental measurements suggested that the adhesion strength, defined as the average normal or shear stress on the interface when pull-off occurs, is on the order of 10-100 kPa between barnacles or ice blocks with such soft substrates[6,14,28]. Since the Young's modulus E for silicone elastomers is on the order of 1MPa[6,14], this range of adhesion strength implies a level of strain that is roughly 1-10%. Therefore, although nonlinear effects associated with large deformation may still be important for cases with strong adhesion, linear elasticity is a relevant assumption to the fouling release or anti-icing applications. The adhesive interaction between the punch and half-space is quantified by the adhesion energy W_{ad} (unit: J/m^2), defined as the energy required to separate a unit area of contact. We assume the interface adhesion to be isotropic, meaning that W_{ad} is independent of the local separation mode, e.g., along the normal or shear directions. In other words, W_{ad} is independent of the mode-mixity of the interface fracture process. As a result, there can be no slip between the punch and the elastic substrate before delamination occurs. This boundary condition is different from the experimental study of Chaudhury and Kim[20] on the shear induced adhesive failure between a rectangular block and a thin PDMS film where the block can slide on the PDMS film before detachment.

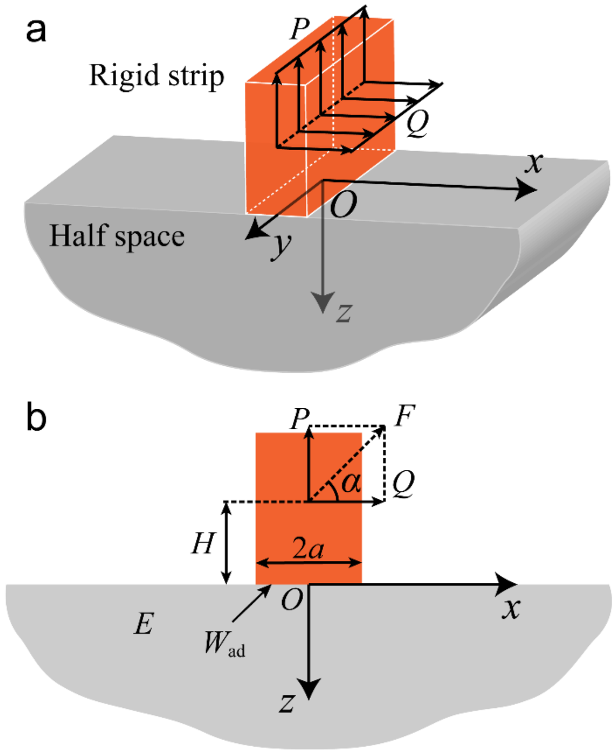

Figure 2 Schematic illustration of a rigid punch bonded to an elastic half-space and subjected to combined shear and normal loadings: (a) three-dimensional and (b) cross-sectional views.

The two line forces P and Q, acting at the midpoint of the punch with a height H above the interface (see Fig.2b), can be combined into a resultant force F that makes an angle α with the x-axis. A positive angle α implies a counterclockwise rotation from the x-axis to the direction of F. The vertical and horizontal components of F, i.e., P and Q, will be referred to as the normal force and shear force hereafter, respectively. Simple geometrical considerations lead to the following equation:

$$Q = F\cos\alpha\,, \quad P = F\sin\alpha\,. \tag{2.1}$$

We emphasize that F, P and Q are "line forces" for which the unit is force per unit length. Next we derive an analytical solution illustrating how the critical force at pull-off, denoted by F_c, depends on mechanical, interface, and geometrical parameters, i.e., E, W_{ad}, a, H and α.

2.2 General solution

Since the punch is assumed to be rigid, either of the two edges of the contact region can be considered as the tip of an interface crack. Whether pull-off occurs is determined by prescribing a fracture criterion at the contact edge, i.e. $G = W_{ad}$ where G is the energy release rate of the interface crack. To evaluate the energy release rate and hence the pull-off force, we first need to determine the tractions within the contact region. As shown in Fig.3a, suppose the elastic half-space is subjected to a distributed normal pressure $p(x)$ and tangential traction $q(x)$ over the contact region ($-a < x < a$). The surface tractions are zero outside the contact region. The displacement components on the surface of the half-space (z =0) due to the tractions $p(x)$ and $q(x)$ are given[35,36]

$$\bar{u}_x(x) = -\frac{2(1-\nu^2)}{\pi E}\int_{-a}^{a} q(s)\ln|x-s|\,ds - \frac{(1-2\nu)(1+\nu)}{2E}\left[\int_{-a}^{x} p(s)\,ds - \int_{x}^{a} p(s)\,ds\right] + B_1, \tag{2.2}$$

$$\bar{u}_z(z) = -\frac{2(1-\nu^2)}{\pi E}\int_{-a}^{a} p(s)\ln|x-s|\,ds + \frac{(1-2\nu)(1+\nu)}{2E}\left[\int_{-a}^{x} q(s)\,ds - \int_{x}^{a} q(s)\,ds\right] + B_2, \tag{2.3}$$

where $\bar{u}_x(x)$ and $\bar{u}_z(x)$ are the horizontal and vertical components of the surface displacement, respectively. The constants B_1 and B_2 need to be determined by choosing a reference datum point on the surface. They can be removed by taking gradients of the displacement components along the surface, which gives,

$$\frac{\partial \bar{u}_x}{\partial x} = -\frac{2(1-\nu^2)}{\pi E}\int_{-a}^{a} \frac{q(s)}{x-s}\,ds - \frac{(1-2\nu)(1+\nu)}{E}p(x), \tag{2.4}$$

$$\frac{\partial \bar{u}_z}{\partial x} = -\frac{2(1-\nu^2)}{\pi E}\int_{-a}^{a} \frac{p(s)}{x-s}\,ds + \frac{(1-2\nu)(1+\nu)}{E}q(x). \tag{2.5}$$

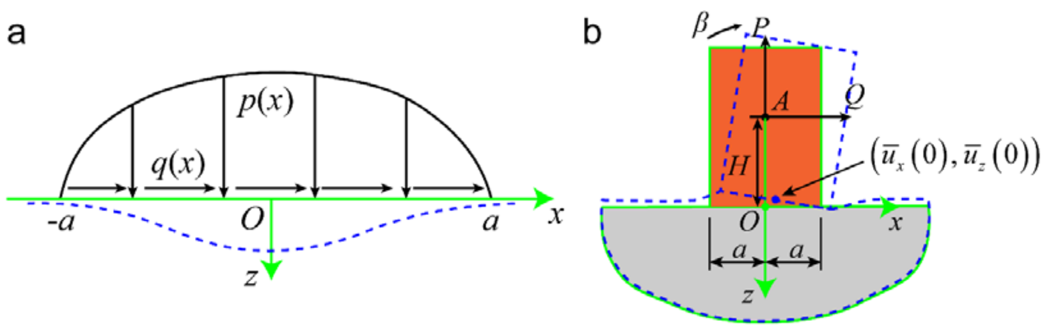

Figure 3 (a) Schematic view of the distributed shear and normal tractions acting on the top surface of the elastic half-space. The deformed surface profile is illustrated by the blue dashed line. (b) Cross-section of the half-space and the punch under external forces. The undeformed and deformed states are illustrated with green solid lines and blue dashed lines, respectively. Point *A* represents the loading position and is located at the *z*-axis with a height *H* above the interface.

Since rigid punch is bonded to the half-space, the surface displacements within the contact region can be specified by the motion of the punch. Specifically, the punch is expected to rotate by a small angle β under combined normal and shear forces (see Fig.3b), which leads to the following expressions for surface displacements,

$$\bar{u}_x(x) = \bar{u}_x(0) - x(1-\cos\beta), \tag{2.6}$$

$$\bar{u}_z(x) = \bar{u}_z(0) + x\sin\beta, \tag{2.7}$$

where $\bar{u}_x(0)$ and $\bar{u}_z(0)$ are surface displacement components at *O* where x=0. Substituting Eqs.(2.6) and (2.7) to Eqs.(2.4) and (2.5) will allow us to solve the surface tractions $p(x)$ and $q(x)$ from a set of coupled integral equations. When the incompressibility of the half-space, i.e., ν=0.5, is assumed, the normal and shear components are decoupled, leading to the following equations for $p(x)$ and $q(x)$:

$$\frac{\partial \bar{u}_x}{\partial x} = 1-\cos\beta = -\frac{3}{2\pi E}\int_{-a}^{a}\frac{q(s)}{x-s}ds, \tag{2.8}$$

$$\frac{\partial \bar{u}_z}{\partial x} = \sin\beta = -\frac{3}{2\pi E}\int_{-a}^{a}\frac{p(s)}{x-s}ds. \tag{2.9}$$

Moreover, equilibrium of the rigid punch implies the following force and moment balance equations:

$$Q = \int_{-a}^{a} q(x)dx, \tag{2.10}$$

$$P = -\int_{-a}^{a} p(x)dx, \tag{2.11}$$

$$QH = \int_{-a}^{a} xp(x)\,dx. \tag{2.12}$$

Note that Eq.(2.12) results from the moment balance of the rigid punch about the point O. Combing Eqs.(2.8)-(2.11), we can obtain the following solutions for the surface tractions:

$$q(x) = -\frac{2E(1-\cos\beta)}{3}\frac{x}{\left(a^2-x^2\right)^{1/2}} + \frac{Q}{\pi\left(a^2-x^2\right)^{1/2}}, -a \le x \le a, \tag{2.13}$$

$$p(x) = \frac{2E\sin\beta}{3}\frac{x}{\left(a^2-x^2\right)^{1/2}} - \frac{P}{\pi\left(a^2-x^2\right)^{1/2}}, -a \le x \le a. \tag{2.14}$$

The angle of rotation β can be solved by substituting Eq.(2.14) into Eq.(2.12), which gives

$$QH = \frac{\pi E a^2}{3}\sin\beta. \tag{2.15}$$

Next we denote normal and shear stress components exposed on the surface of the elastic half-space as $\bar{\sigma}_z(x) \equiv \sigma_z(x, z=0)$ and $\bar{\tau}_{xz}(x) \equiv \tau_{xz}(x, z=0)$. Using Eqs.(2.13)-(2.14), we obtain

$$\bar{\sigma}_z(x) = -p(x) = -\frac{2QH}{\pi a^2}\frac{x}{\left(a^2-x^2\right)^{1/2}} + \frac{P}{\pi\left(a^2-x^2\right)^{1/2}}, -a \le x \le a, \tag{2.16}$$

$$\bar{\tau}_{xz}(x) = -q(x) = -\frac{Q}{\pi\left(a^2-x^2\right)^{1/2}}, -a \le x \le a, \tag{2.17}$$

where we have applied the infinitesimal deformation assumption that $\beta \ll 1$ and retained only the first order terms of β. Specifically, the first term of $q(x)$ is proportional to $(1-\cos\beta) \sim \beta^2$ and thus is neglected in Eq.(2.17), while the coefficient $2E\sin\beta/3$ in the first term of $p(x)$ is substituted by $2QH/\pi a^2$ using Eq.(2.15). The two equations above show that both the normal and shear stress components exhibit a square root singularity at the contact edges $x = \pm a$. This is because the contact edge is equivalent to the tip of an interface crack between the rigid punch and the elastic half-space. Note that the stress field near the tip of an interface crack often exhibits an oscillatory singularity[37], which is not present here because the substrate is incompressible (ν =1/2) and the oscillation is removed[16]. The Mode I and II stress intensity factors, denoted by K_I and K_{II} respectively, at the two bonding edges $x = \pm\, a$ can be calculated as follows:

$$K_I^{(a)} = \lim_{x\to a} \bar{\sigma}_z\left(x\right)\sqrt{2\pi\left(a-x\right)} = -2\frac{Q}{\sqrt{\pi a}}\frac{H}{a} + \frac{P}{\sqrt{\pi a}}, \tag{2.18}$$

$$K_{II}^{(a)} = \lim_{x\to a} \bar{\tau}_{xz}\left(x\right)\sqrt{2\pi\left(a-x\right)} = -\frac{Q}{\sqrt{\pi a}}, \tag{2.19}$$

$$K_I^{(-a)} = \lim_{x\to(-a)} \bar{\sigma}_z\left(x\right)\sqrt{2\pi\left(a+x\right)} = 2\frac{Q}{\sqrt{\pi a}}\frac{H}{a} + \frac{P}{\sqrt{\pi a}}, \tag{2.20}$$

$$K_{II}^{(-a)} = \lim_{x\to(-a)} \bar{\tau}_{xz}\left(x\right)\sqrt{2\pi\left(a+x\right)} = -\frac{Q}{\sqrt{\pi a}}. \tag{2.21}$$

These expressions of the K_I and K_{II} allow us to evaluate the energy release rate at the two contact edges based on the following equation[16]:

$$G = \left(\frac{1-\nu^2}{2E}\right)\left(K_I^2 + K_{II}^2\right). \tag{2.22}$$

Using Eqs.(2.18)–(2.21) and setting the Poisson's ratio ν=0.5, we obtain the following results for the strain energy release rates at $x = \pm a$:

$$G^{(-a)} = \frac{3}{8\pi a E}\left(\left(\frac{2QH}{a}+P\right)^2 + Q^2\right) \text{ and } G^{(a)} = \frac{3}{8\pi a E}\left(\left(-\frac{2QH}{a}+P\right)^2 + Q^2\right). \tag{2.23}$$

Without loss of generality, we assume both P and Q to be positive, which implies that $G^{(-a)} > G^{(a)}$. As a result, delamination should initiate at the left edge where $x = -a$. Recalling that the interfacial adhesion energy is by W_{ad} and the substrate is elastic, the onset of delamination occurs when $G^{(-a)} = W_{ad}$. Using Eq.(2.1), we obtain the following equation for the critical force F_c to initiate delamination:

$$F_c = \sqrt{\frac{2\pi a E W_{ad}}{3\left(\frac{H^2}{a^2}\cos^2\alpha + \frac{H}{a}\cos\alpha\sin\alpha + \frac{1}{4}\right)}}, \tag{2.24}$$

where α is the angle of the combined force F in Fig.2b ($0 \leq \alpha \leq \pi/2$). Note that F_c is a monotonically decreasing function of the contact width a. This implies that the delamination process is unstable under force control once it initiates at the contact edge. Therefore, the F_c in Eq.(2.24) is the pull-off force we are looking for.

2.3 Pull-off force

Although we have assumed that the delamination process is independent of the local fracture modes at the contact edge, i.e., W_{ad} is mode-independent, the pull-off force does depend on the mode of delamination, represented by the direction α and height H of the delamination force F. For example, under normal separation where $\alpha = \pi/2$, the pull-off force, denoted by P_c, is

$$P_c = \sqrt{\frac{8\pi a E W_{ad}}{3}}. \tag{2.25}$$

On the other hand, under shear delamination where angle $\alpha = 0$, the pull-off force Q_c given by Eq.(2.24) is

$$Q_c = \sqrt{\frac{8\pi a E W_{ad}}{3\left(4\dfrac{H^2}{a^2}+1\right)}}. \tag{2.26}$$

Interestingly, the shear pull-off force Q_c is smaller than the normal pull-off force P_c except when H=0.

To further illustrate the effect of H and α on the pull-off force F_c, we use the normal pull-off force P_c as the benchmark to define the following normalized pull-off force:

$$\bar{F}_c = \frac{F_c}{P_c} = \sqrt{\frac{1}{\left(4\dfrac{H^2}{a^2}\cos^2\alpha + 4\dfrac{H}{a}\cos\alpha\sin\alpha + 1\right)}}. \tag{2.27}$$

The fact that $\bar{F}_c \leq 1$ implies that normal delamination requires the largest pull-off force. Figure

4 shows a 3D surface plot of the normalized pull-off force versus α and H, as well as the dependence of pull-off force on α for different values of H/a.

We first observe that $\overline{F}_c$ is a monotonically decreasing function with increasing H. This is because the shear component Q of the delamination force can cause the punch to rotate in the clockwise direction. Larger H results in a larger torque by Q and hence larger rotation. Such rotation can modify the local mixed-mode fracture conditions at the two contact edges ($x = \pm a$) by developing an extra normal stress at the interface that decays from the left contact edge to the right one. This effect, under a special case of α =0 (i.e., shear delamination), has been discussed in Chaudhury and Kim[20]. It can create an uneven distribution of energy release rate (see Eq.(2.23)), and cause the delamination to initiate only at the left contact edge ($x = -a$). In contrast, under a pure normal force, both contact edges are subjected to the same energy release rate, and thus will experience delamination simultaneously. This mechanism causes F_c to decrease with increasing H. When H=0, $\overline{F}_c$ =1 regardless what the angle α is. In this particular case, the punch does not rotate, and the energy release rates at both contact edges are equal to each other. The angle α can only affect the mode-mixity conditions at the two contact edges. However, since we have assumed W_{ad} is independent of the local mixed-mode condition, the pull-force becomes independent of α and is equal to the normal pull-off force P_c.

Next we discuss the effect of angle α. The normalized pull-off force $\overline{F}_c$ is not a monotonic function of α. Indeed, we find that $\overline{F}_c$ reaches the following minimum:

$$\overline{F}_{c\_\min} = \sqrt{1+\left(\frac{H}{a}\right)^2} - \frac{H}{a}, \tag{2.28}$$

when α is equal to α_m below:

$$\alpha_m = \tan^{-1}\left(\sqrt{1+\left(\frac{H}{a}\right)^2} - \frac{H}{a}\right). \tag{2.29}$$

This implies that for a given value of H/a, the direction of the delamination force can be adjusted to minimize the pull-off force according to Eq.(2.29). For example, the angle α_m

required to minimize the pull-off force would decrease to 0 as *H/a* approaches infinity, meaning that in the limit of large *H/a,* the shear delamination mode (α =0) should be applied to minimize the pull-off force.

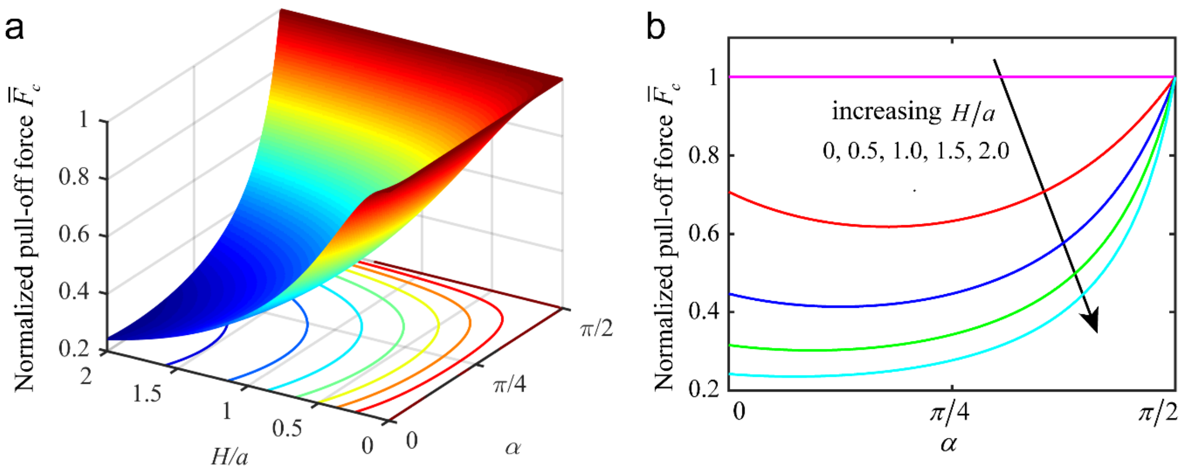

Figure 4 (a) Contour plot of the normalized pull-off force versus *H/a* and α. (b) The dependence of the pull-off force on α for different values of *H/a*.

In this section we have used a 2D plane strain model to understand how the pull-off force depends on the mode of delamination, represented by the angle α and loading position *H*. The analytical solutions obtained in this section can be potentially used to guide the design of delamination modes to enhance or reduce the pull-off force. Moreover, the fundamental insights established in this section will also help us understand the 3D delamination behaviors to be considered in Section 3 and 4.

3. Finite element model: 3D simulations

3.1 Model description

In this section, we consider the delamination process of a rigid cylindrical punch from an elastic substrate under normal and shear forces, as schematically shown in Fig.5a. Here we assume the substrate has a finite thickness *h* and is bonded to a rigid backing surface. This is motivated by the fact that in practice the FRC or anti-icing coatings are usually supported by a stiff surface, and the coating thickness is comparable or even smaller than dimensions of the adhering objects (e.g. barnacles or ice blocks). Therefore, the half-space assumption may not always be satisfied for practical applications and the effect of finite substrate thickness needs to be accounted for.

The existing solutions for pull-off forces reviewed in Section 1 focused on normal delamination, where one can take advantage of axisymmetry to solve the interface fracture problem into a 2D domain. In our case, the combined normal and shear forces would induce a 3D stress and strain fields in the elastic substrate, which is difficult to solve analytically. Therefore, we resort to numerical simulations and build an FE model in ABAQUS (v6.14, Simulia Inc, Providence, RI) to calculate the pull-off force. Figure 5b shows the finite element model wherein the symmetry allows us to simulate a half of the cylinder and substrate. The cylindrical punch is modeled as a discrete rigid body, and the soft substrate with Young's modulus E is modeled as an incompressible neo-Hookean solid. The substrate is meshed into 263080 C3D8RH elements and 920 C3D6H elements. We have performed mesh convergence test (see Appendix 1) to ensure mesh independence of our results. The adhesive interaction on the contacting interface is described by a cohesive zone model[38], which will be discussed in Section 3.2. Regarding boundary conditions, the circumferential and bottom surfaces of the substrate are fixed, and the lateral cross-section exposed by the symmetry cut is subjected to the symmetry boundary condition, i.e., no normal displacements and no shear tractions. The delamination force is applied to the cylindrical punch, and the point of action is located on the central axis of the punch with a height H above the substrate surface (see Fig.5b). To make sure that the delamination process is not affected by the circumferential boundary of the substrate, the radius of the substrate is set to be 10 times of the punch radius.

Since the punch may become tilted forward due to the shear force during delamination, its front edge can be pressed into the substrate, which may cause severe local stress concentrations and mesh distortion. To resolve this problem, we introduce a fillet of $0.1r$, where r denotes the punch radius, at the bottom edge of the punch (see inset of Fig.5b). As a result, the contact radius is 0.9*r* rather than *r*. We will denote the contact radius as *a* to maintain consistency with notations of the plane strain model. Since the punch is rigid, introduction of the fillet does not affect the local stress states near the delamination site (see inset of Fig.5a). Therefore, the delamination behavior and pull-off force is independent of the fillet.

We use the dynamic implicit solver in ABAQUS to capture the rapid unloading once the delamination process is initiated. In addition, we adopt displacement-controlled loading to stabilize the simulation, namely that a prescribed displacement along the desired angle α, instead of a prescribed force, is applied to the punch, while other degrees of freedom of the rigid punch (e.g. rotation) are unconstrained. A local Cartesian coordinate system with one axis aligned with the loading direction is used to ensure that the direction of delamination force is kept constant throughout the entire simulation. The main advantage of the displacement controlled loading is that it can capture pull-off force and the subsequent delamination much more efficiently than the force controlled loading.

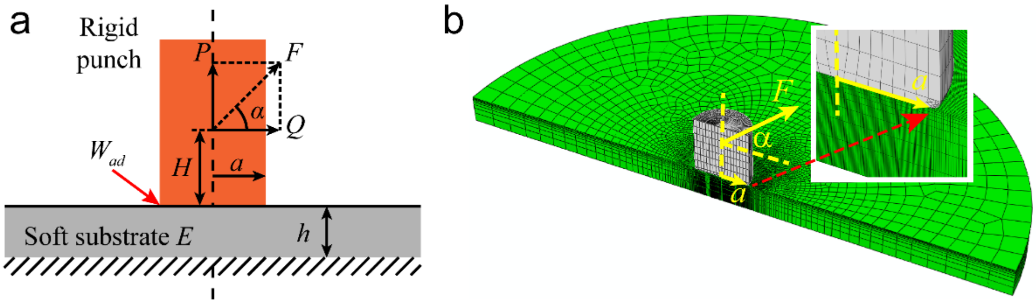

Figure 5 (a) Schematic of a cross-section of a cylindrical rigid punch adhering to a finite-thickness soft substrate with the bottom surface being fixed. The applied force and thus the deformation of the substrate are non-axisymmetric. (b) 3D mesh of FE model of the punch and the substrate with a representative thickness. The symmetry of the model allows us to perform the simulation by using the half-model. The inset shows the fillet of the punch. The cylinder radius subtracted by the fillet radius is defined as *a*.

3.2 Cohesive zone model

The cohesive zone model is defined by prescribing a relation between the mechanical traction on the interface and the relative separation between the two contacting surfaces. Complete interface failure occurs when the maximum separation δ_f is reached and the traction reduces to 0. The energy required to achieve complete interface failure of a unit contacting area is defined as the adhesion energy W_{ad}. In general, the global delamination behavior, e.g. the pull-off force, is insensitive to the detailed shape of the traction-separation curve, as long as W_{ad} is kept constant and the maximum separation δ_f is much smaller than the characteristic length scales of the contacting region[38]. Therefore, we adopt a simple bi-linear traction-separation law for our cohesive zone model, which is illustrated in Fig.6. The adhesion energy W_{ad} is equal to the area underneath the traction-separation curve. To validate our cohesive zone model, we tested the effects of different parameters for the cohesive zone model. Using normal delamination as a benchmark example, we find that the pull-off forces predicted by our simulations based on the following cohesive zone parameters agree well with those given by Yang and Li[17]:

$$\delta_0 = \frac{1}{2}\delta_f = \frac{W_{ad}}{\sigma_{\max}}, \frac{\delta_f}{a} = 0.01. \quad (3.1)$$

These parameters will be used throughout our simulations. Note that the element size within the contacting area is selected to be smaller than δ_f to ensure mesh convergence within the cohesive zone.

To identify the extent of partial interface separation in the simulations, we use a damage variable D defined by the cohesive zone model. This variable D ranges from 0 to 1, with 1 representing complete separation. Let δ_m represent the maximum separation of the cohesive zone attained in the loading history. When δ_m is less than δ_0 (i.e., the separation at peak stress; see Fig.6), damage does not occur and D =0. Damage is initiated once $\delta_m > \delta_0$ and D is calculated according to the linear evolution model:

$$D = \frac{\delta_f\left(\delta_{\mathrm{m}} - \delta_0\right)}{\delta_{\mathrm{m}}\left(\delta_f - \delta_0\right)}. \quad (3.2)$$

In a 3D model, the traction-separation relation needs to be defined along three directions: one normal to the interface and the other two tangential to the interface. Here, we assume an isotropic interfacial behavior with respect to three directions. The damage initiation is governed by a quadratic stress criterion which requires

$$\left(\frac{\sigma_n}{\sigma_{\max}}\right)^2+\left(\frac{\sigma_s}{\sigma_{\max}}\right)^2+\left(\frac{\sigma_t}{\sigma_{\max}}\right)^2=1, \quad (3.3)$$

with σ_n, σ_s, σ_t representing the normal and the two shear tractions, respectively, and the damage behavior in mixed mode are described by the built-in power law with the exponent of 2, i.e.,

$$\left(\frac{W_n}{W_{ad}}\right)^2+\left(\frac{W_s}{W_{ad}}\right)^2+\left(\frac{W_t}{W_{ad}}\right)^2=1, \quad (3.4)$$

where W_n, W_s and W_t represent the work done by the normal and the two shear adhesive stresses, respectively.

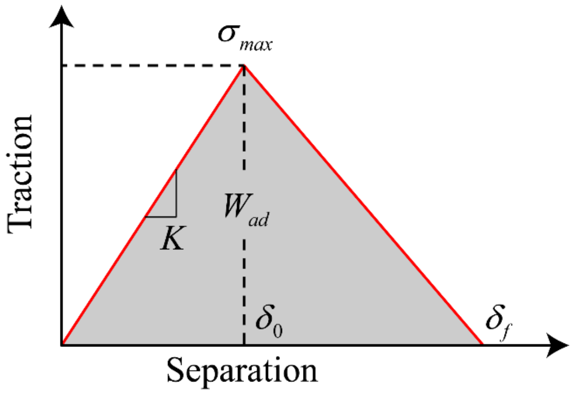

Figure 6 An example of the traction-separation law for the cohesive zone model.

3.3 Model parameters and dimensional analysis

The FE model described above involves a number of material and geometrical parameters: substrate Young's modulus E, substrate thickness h, contact radius a, height of delamination force H, angle of delamination force α, and adhesion energy W_{ad}. Here we perform a dimensional analysis to reduce the number of independent parameters. First, we use the π theorem to get

$$\frac{F_c}{Ea^2} = g\left(\frac{W_{ad}}{Ea}, \frac{a}{h}, \frac{a}{H}, \alpha\right), \tag{3.5}$$

where F_c is the pull-off force and g is an unknown function. To further simplify this equation, we assume infinitesimal deformation so that the elastic substrate can be considered as a linear system represented by a compliance C with

$$\Delta = CF, \tag{3.6}$$

where F is the force applied to the punch and Δ is the corresponding displacement. Following Kendall[15], we can derive the following expression for the total potential energy of the system (punch + substrate):

$$U_T = \frac{1}{2}F\Delta - F\Delta - AW_{ad} = -\frac{CF^2}{2} - AW_{ad}, \tag{3.7}$$

where A is the contact area. Initiation of delamination requires the following equation to be satisfied:

$$\frac{\partial U_T}{\partial A} = -\frac{F_c^2}{2}\frac{\partial C}{\partial A} - W_{ad} = 0. \tag{3.8}$$

Since $\partial C/\partial A$ is independent of the adhesion energy W_{ad}, Eq.(3.8) suggests that the pull-off force F_c scales with $W_{ad}^{1/2}$. Using this scaling and Eq.(3.5), we can write

$$\frac{F_c}{Ea^2} = \sqrt{\frac{W_{ad}}{Ea}}\, g^*\left(\frac{a}{h}, \frac{H}{a}, \alpha\right) \quad \text{or} \quad F_c = \sqrt{Ea^3 W_{ad}}\, g^*\left(\frac{a}{h}, \frac{H}{a}, \alpha\right). \tag{3.9}$$

The scaling relation in Eq.(3.9) will be used to guide our interpretation of the pull-off force data in Section 4.

4. Results and Discussions

In this section we present the FE results for the pull-off force F_c under various geometric and loading conditions and, more importantly, the adhesion mechanics underlying the pull-off forces. Eq.(3.9) motivates us to define a normalized pull-off force to reduce the number of independent parameters. Similar to the plane strain case in Section 2, we use the pull-off force F_{c0} for an elastic half-space (a/h =0) under normal separation ($\alpha = \pi/2$) as the reference. According to Eq.(1.1)[15], F_{c0} for an incompressible substrate is

$$F_{c0} = \sqrt{\frac{32\pi E a^3 W_{ad}}{3}}, \tag{4.1}$$

which yields the following definition of normalized pull-off force

$$\bar{F}_c = \frac{F_c}{F_{c0}} = \sqrt{\frac{3}{32\pi E a^3 W_{ad}}} F_c = \sqrt{\frac{3}{32\pi}} g^*\left(\frac{a}{h}, \frac{H}{a}, \alpha\right). \tag{4.2}$$

The three independent parameters are: a/h representing the substrate thickness, H/a representing the location of loading point, and α representing the angle of delamination force.

4.1 Normal separation

We first consider the case of normal separation as a benchmark to validate our FE model, since it has been solved in a number of previous theoretical analyses[15,17,21,31]. For normal separation, $\alpha = \pi/2$ and the delamination process is independent of the height H of loading point. Therefore, $\bar{F}_c$ is only a function of a/h. Figure 7 shows the FE results (symbols) of $\bar{F}_c$ under normal separation for different values of a/h. Also plotted in Fig.7 are existing analytical solutions in the literature. Specifically, Yang and Li[17] performed a rigorous analysis based on which numerical solutions of the pull-off force were obtained for different substrate thicknesses as showed by the red solid line. On the other hand, Shull and Crosby[31] first used FE simulations to obtain an empirical expression for the compliance of the punch/substrate system, based on which the pull-off force is determined by evaluating the energy release rate and setting it equal to the adhesion energy W_{ad}. This resulted in an analytical formula for the pull-off force as follows:

$$F_c = 6.70\sqrt{E a^3 W_{ad}}\left[\frac{0.75 + (a/h) + (a/h)^3}{\left(0.75 + 2(a/h) + 4(a/h)^3\right)^{1/2}}\right]. \tag{4.3}$$

Note that both solutions (i.e., Yang and Li[17] and Shull and Crosby[31]) adopted for comparison here are based on the assumption of no-slip interface between the punch and the substrate and between the substrate and the backing surface. As described in Section 1, Yang and Li[17] also considered other cases of frictional boundary conditions. These solutions are not discussed here since they are based on different interface conditions from our FEM model.

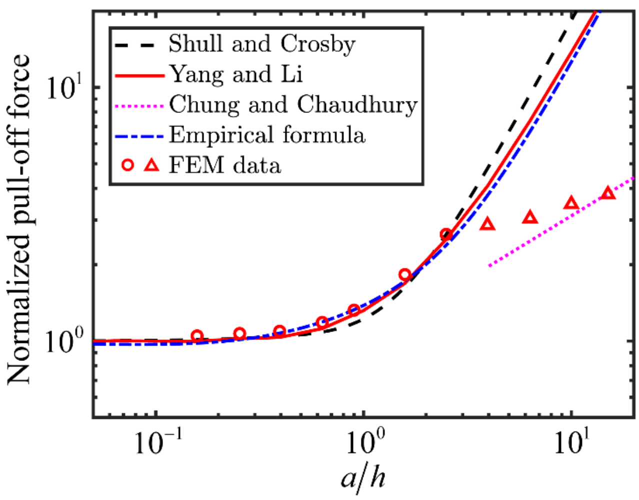

Figure 7 Normalized pull-off force versus *a/h* under normal separation. The symbols (circles: Mode-I crack propagation; triangles: interface cavitation) represent our FE results. The black dashed line is obtained by the empirical solution of Shull and Crosby[31] and the red solid line is obtained by the numerical solution of Yang and Li[17]. Our empirical formula, Eq.(4.4), is plotted as the blue dash-dot line. The magenta dotted line illustrates the solution of Chung and Chaudhury[21] which accounts for interface cavitation with thin substrates.

As can be seen in Fig.7, both Eq.(4.3) by Shull and Crosby[31] and the numerical solutions by Yang and Li[17] agree well with our FE results for substrate with large to moderate thickness ($a/h \leq 2.5$). Interestingly, for thin substrate ($a/h > 2.5$), our FE results are significantly lower than the theoretical predictions of either Yang and Li[17] or Shull and Crosby[31]. This is because in both of these studies, the delamination is assumed to initiate at the periphery of the circular contact region, followed by an unstable Mode-I crack propagation inward, consistent with what we observed in FE simulations for thick substrates. An example where $a/h = 0.9$ is illustrated in Fig.8d, where the color map of the interface damage variable D (see Eq.(3.2)) is plotted to illustrate the evolution of delaminated region. Recall that D ranges from 0 to 1, with 1 denoting complete delamination. The pull-off force occurs when delamination started at the outer edge of the contact area (marked by "N_1" in Fig.8a and 8d). In contrast, for thinner substrates ($a/h \geq 3.95$), the delamination does not initiate at the periphery but rather occurs through interface cavitation. Specifically, when a/h =3.95, Fig.8e shows that delamination first occurs in the center of the contact area and then propagates outward. When the substrate thickness is further reduced (a/h =10), multiple cavities may first be formed within the contact area, and then grow into a larger delaminated region (see Fig.8f). These behaviors found in our simulation results are consistent with the three normal delamination modes, i.e. edge crack propagation, internal crack propagation and interface cavitation, experimentally observed in Crosby et al.[23] and Webber et al.[24].

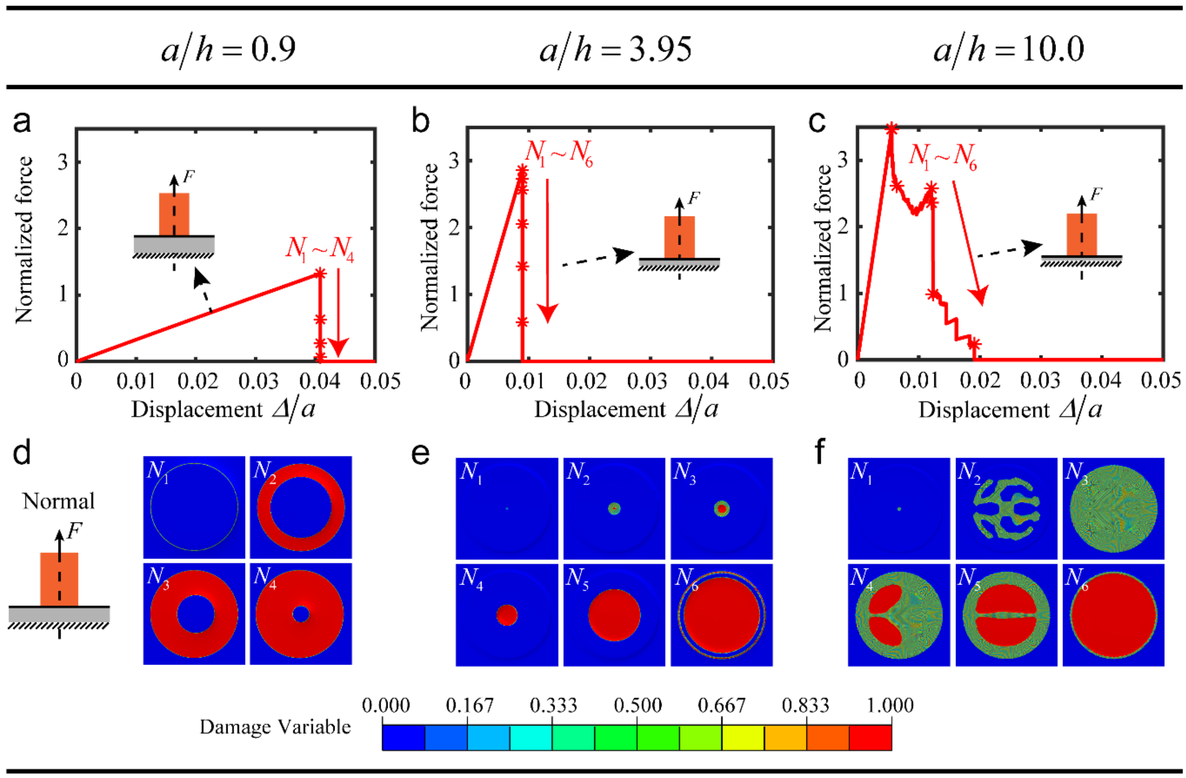

Figure 8 Delamination behavior under normal separation with different a/h. (a-c) The force-displacement curves during delamination. (d-f) Evolution of the interface damage variable D (shown in the top view of the substrate surface) to quantify local interface delamination: (d) a/h = 0.9, (e) a/h = 3.95, (f) a/h = 10.0.

The underlying physical mechanism of interface cavitation has been studied in the literature[16,26,39]. Briefly, the incompressibility of the substrate, together with the small thickness and fixed boundary condition at the bottom of the substrate, can lead to a hydrostatic tensile stress state within the contact area[16]. In addition, as a/h approaches infinity and assuming perfectly bonded interface, the normal stress within the contact area was found to be[33,39,40]: $\sigma_{zz}(r) = (2F/\pi a^2)(1-r^2/a^2)$ based on a first order asymptotic analysis[40]. This solution indicates that the normal stress decays as one moves away from the center of the contact region. However, near the contact edge there exists a boundary layer where the normal stress exhibits a singularity, because the contact edge is equivalent to the tip of an interface crack between the rigid punch and the elastic substrate[16]. This would lead to a steep upturn of the normal stress within the boundary layer. The size of the boundary layer is bounded by the substrate thickness h and thus should decrease as the substrate becomes thinner[41]. Note that a cohesive zone model is implemented at the punch/substrate interface in our FEM simulations. For thin substrates (i.e., large a/h), the small boundary layer at the contact region is covered by the cohesive zone, which regulates the theoretically predicted stress singularity by allowing partial interface separation. The cohesive zone model may also affect the normal stress distribution by introducing an additional interface compliance[42]. Nevertheless, the increased normal stress towards the center of the contact region as the substrate becomes thinner tends to promote a surface instability that causes local delamination and hence interface cavitation[21,27,43]. To distinguish the two delamination modes, i.e., unstable crack propagation or interface cavitation, in Fig.7 we use triangular symbols to represent the FE data of pull-off force for cases with interface cavitation while circular symbols for cases where delamination is dominated by Mode-I crack propagation. Chung and Chaudhury[21] derived a solution for the pull-off force that accounts for interface cavitation through an energy minimization method. This solution, shown in Eq.(1.6) and plotted in Fig.7, is consistent with our FE data as the substrate becomes thinner (or a/h increases). However, our FE data do exhibit a slightly different scaling relation between $\overline{F}_c$ and a/h from that predicted by Chung and Chaudhury[21]. We emphasize that since interface cavitation involves a surface instability of the substrate, the development of cavitation may be sensitive to the imperfections within the FE model. In our model, imperfections were not deliberately seeded into the simulations, but rather came from the geometric irregularities of the mesh. A systematic study on the effects of imperfections is required to achieve quantitative conclusions on the pull-off force with interface cavitation, which is beyond the scope of this paper. Therefore, our focus will be placed on cases where delamination is dominated by interface crack propagation.

Finally, we modify Eq.(3.4) to the following form to obtain a more accurate formula for the normal pull-off force:

$$F_c = C_1\sqrt{Ea^3W_{ad}}\left[\frac{0.75+C_2\left(a/h\right)+C_3\left(a/h\right)^3}{\left(0.75+C_4\left(a/h\right)+C_5\left(a/h\right)^3\right)^{1/2}}\right], \tag{4.4}$$

where C_1 to C_5 are constant coefficients. To ensure that Eq.(4.4) recovers Eq.(4.1) when $a/h \ll 1$ and Eq.(1.5) when $a/h \gg 1$, we impose two constraints: $C_1 = 8\sqrt{2\pi}/3$ and $C_1C_3/\sqrt{C_5} = \pi/\sqrt{2}$. By fitting Eq.(4.4) to the numerical results of Yang and Li[17] (red solid line in Fig.7), we found that C_2= 2.2002, C_3= 0.2684, C_4= 5.8186, and C_5= 0.7427 (also summarized in Table 1). In the next section we will show that Eq.(4.4) can also be used to fit the pull-off force data for some shear separation cases.

4.2 Shear separation

In this section, we consider shear separation (α =0) and focus on computing the pull-off force for different substrate thicknesses (*a*/*h*) and loading positions (*H*/*a*) and understanding the corresponding delamination mechanisms.

4.2.1 Cases with large H/a

We start with cases with large *H*/*a*. Specifically, Fig.9 plots the normalized pull-off force $\overline{F}_c$ defined in Eq.(4.2) versus *a*/*h* for *H*/*a* = 1.11 and 1.67. The normalized pull-off force under normal separation is also plotted as a reference for comparison. Clearly the pull-off force under shear separation is much lower than that under normal separation. In addition, shear separation with a larger H/a results in a smaller pull-off force.

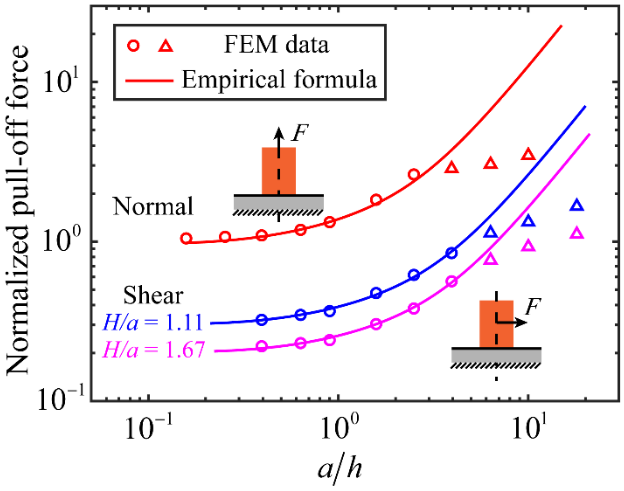

Figure 9 Normalized pull-off force versus a/h under shear separation with H/a =1.11 and 1.67. The normal separation case is also included for comparison. The symbols (circles: Mode-I crack propagation; triangles: interface cavitation) represent our FE results. The solid lines are obtained by fitting Eq.(4.4) to the FE data with the corresponding coefficients given in Table 1.

To understand the mechanism underlying the lowered pull-off force, the evolution of delamination for H/a =1.11 and three representative substrate thickness (a/h =0.9, 3.95, 10) are illustrated in Fig.10 using the color maps of the interface damage variable D. For thick substrate (e.g., a/h =0.9), unlike normal separation where delamination initiates along the periphery of the contact area (see Fig.8d), Fig.10d shows that delamination initiates at the left edge of the contact area, followed by an unstable growth of delaminated region across the contact area (assuming force control). Such localized delamination, caused by rotation of the rigid punch driven by the rigid punch and the consequent stress concentration at the left edge, leads to the lower pull-off force under shear separation. This mechanism also implies that increasing H/a can reduce the pull-off force by promoting rotation of the punch, which is consistent with our observations in the simulation. When the substrate becomes very thin (e.g., a/h =10), interface cavitation can be observed in Fig.10f, but is biased towards the left edge due to the stress concentration caused by punch rotation. In Fig.9 we use triangular and circular symbols to denote the FE data for pull-off forces with and without interface cavitation, respectively. Similar to normal separation, the triangular symbols are much lower than the trend extrapolated from the circular symbols, indicating that interface cavitation can also reduce the pull-off force under shear separation.

Since the shear separation with thick substrates is governed by local Mode-I interface crack propagation, the pull-off force data for shear separation in Fig.9 follow the similar trend as the pull-off force for normal separation. Indeed, we find that the shear pull-off force data can be well captured by shifting the normal pull-off force curve in the log-log plot of Fig.9. This enables a simple way of obtaining empirical pull-off force formulas for the shear separation cases by rescaling $\bar{F}_c$ and a/h based on the shifting factors. As a result, we find that the pull-off force data under shear separation (circular symbols in Fig.9) can still be well captured by Eq.(4.4), and the corresponding values of C_1 to C_5 are listed in Table 1 below.

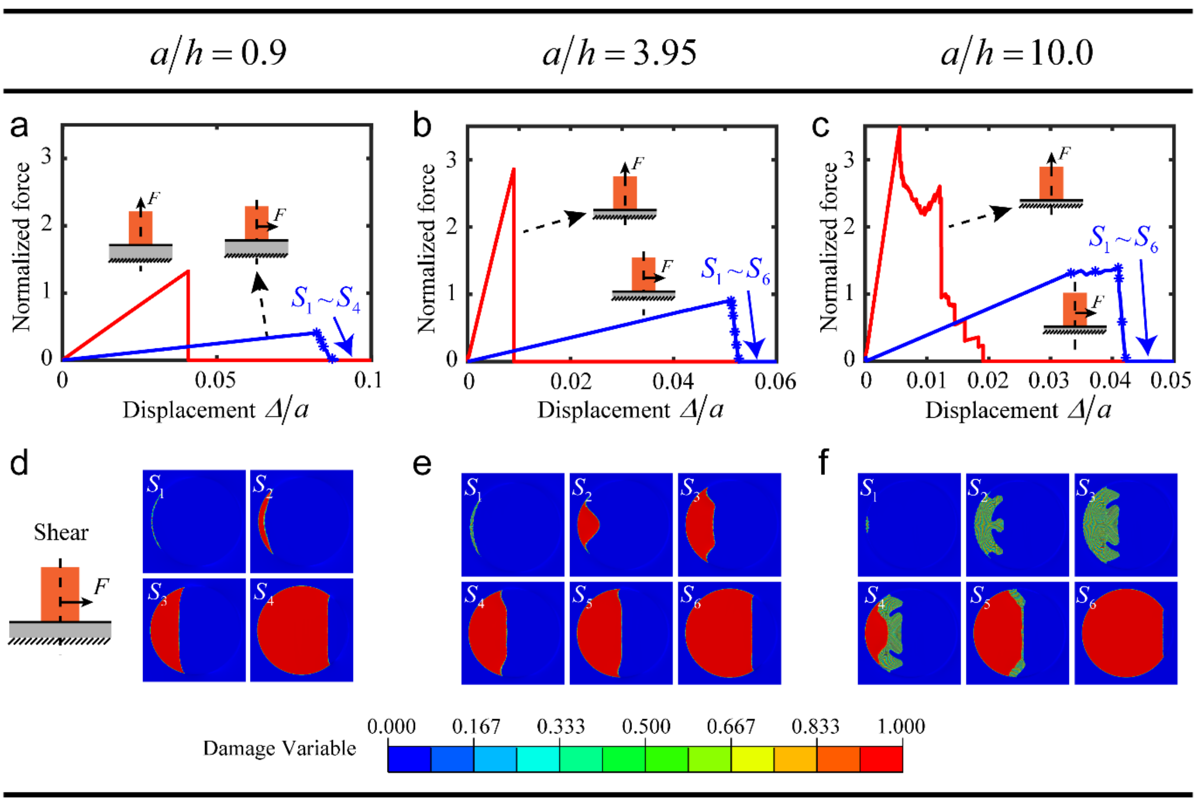

Figure 10 Delamination behavior under shear separation with H/a=1.11 and different a/h. (a-

c) The force-displacement curves during delamination. The corresponding force-displacements for normal separation is included for comparison. (d-f) Evolution of the interface damage variable D (shown in the top view of the substrate surface) to quantity local interface delamination: (d) a/h = 0.9, (e) a/h = 3.95, (f) a/h = 10.0.

Table 1: Coefficients for the empirical formula Eq.(4.4) of pull-off force under normal or shear separation.

H/a	**Valid for**	C_1	C_2	C_3	C_4	C_5
			Normal separation			
For any H/a	$a/h \leq 2.5$	$\frac{8}{3}\sqrt{2\pi}$	2.2002	0.2864	5.8186	0.7427
			Shear separation			
1.67	$a/h \leq 3.95$	1.3973	1.5663	0.1033	4.1422	0.2680
1.11	$a/h \leq 3.95$	2.0892	1.6472	0.1202	4.3562	0.3117
0.56	$a/h \leq 1.58$	3.9992	1.6715	0.1256	4.4204	0.3256

4.2.2 Cases with small H/a

Besides the two delamination modes discussed above (i.e., Mode-I crack propagation and interface cavitation), a new delamination mode for shear separation emerges if H/a is further decreased. To see that, we plot the normalized pull-off force versus a/h for three cases of H/a (= 0.56, 0.28, 0) in Fig.11. Specifically, when H/a =0.56, the pull-off force follows the empirical formula in Eq.(4.4) for substrates with large to moderate thickness ($a/h \leq 1.58$). The corresponding fitting parameters are listed in Table 1. However, for thin substrates ($a/h \geq 2.5$), the pull-off force data points deviate from the trend given by Eq.(4.4) (see Fig.11). To understand the physical nature of this deviation, the evolution of interface delamination for H/a =0.56 and three cases of a/h (= 0.9, 2.5, 10.0) is shown in Fig.12a. Interestingly, when the substrate is thick (a/h =0.9), we observe the same delamination process illustrated in Fig.10d, i.e., delamination initiates at the left edge of the contact area due to rotation of the punch and then spreads across the entire contact area. In contrast, when the substrate is thin (a/h =2.5 or

10), delamination initiates at both the top and bottom edges of the contact area. This is because thin substrate is much less compliant along the normal direction, which suppresses the punch rotation under the delamination force *F*. As a result, the contacting area is primarily subjected to shear tractions, and thus delamination is mainly due to a Mode-II interface crack propagation. We will refer to this mode as Mode-II crack propagation.

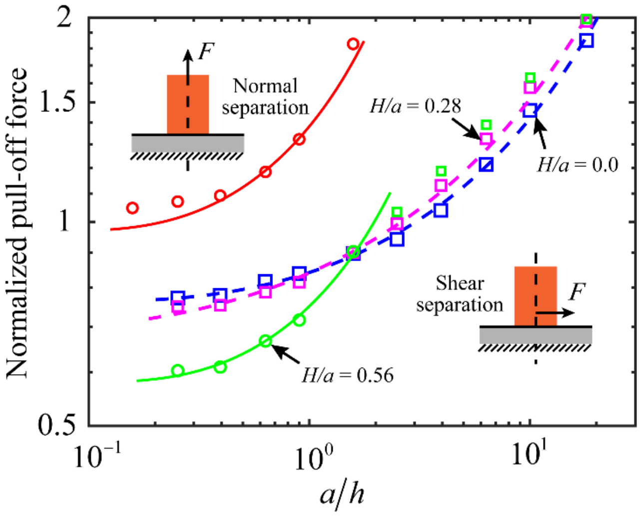

Figure 11 Normalized pull-off force versus *a/h* under shear separation with *H/a* =0, 0.28 and 0.56. The normal separation case is also included for comparison. The symbols (circles: Mode-I crack propagation; squares: Mode-II crack propagation) represent our FE results. The solid lines are obtained by fitting Eq.(4.4) to the FE data with the corresponding coefficients given in Table 1. The dashed lines are given by Eq.(4.5) and Eq.(4.6).

When *H/a* is further reduced (i.e., 0.28 and 0 in Fig.11), the Mode-II crack propagation mode prevails and the pull-off force becomes insensitive to *H/a*. In particular, Fig.12b shows that when *H/a* =0, delamination always initiates at the top and bottom edges even for thick substrate (*a/h* =0.9). In this mode, the empirical formula in Eq.(4.4) can no longer capture the FE data of pull-off forces. Instead, we find that the following expression by modifying the form of Eq.(4.4) and fitting the FE data for *H/a* =0 and 0.28 in Fig.11, respectively:

$$F_c = 5.2537\left(W_{ad}Ea^3\right)^{1/2}\left[\frac{0.75+0.8519(a/h)^{0.64}+0.0166(a/h)^{1.93}}{\left(0.75+2.253(a/h)^{0.64}+0.0431(a/h)^{1.93}\right)^{1/2}}\right], \quad H/a=0.0 \quad (4.5)$$

$$F_c = 4.7616\left(W_{ad} E a^3\right)^{1/2}\left[\frac{0.75+1.3492\left(a/h\right)^{0.55}+0.066\left(a/h\right)^{1.65}}{\left(0.75+3.5682\left(a/h\right)^{0.55}+0.1713\left(a/h\right)^{1.65}\right)^{1/2}}\right], H/a=0.28. \quad (4.6)$$

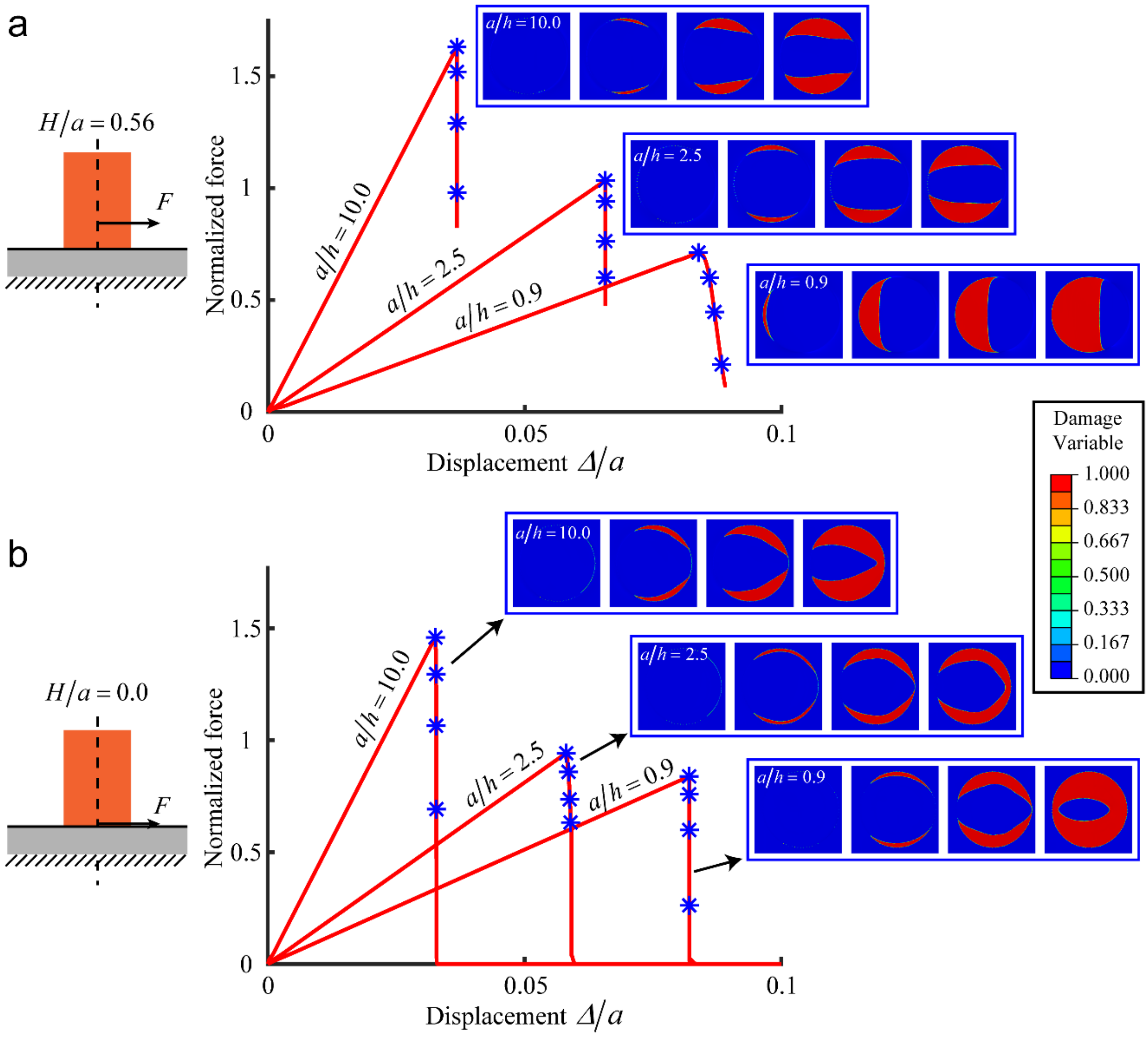

Figure 12 The force-displacement curves and the corresponding evolutions of interface delamination (represented by the color map of damage variable D) for small values of H/a: (a) H/a=0.56 and (b) H/a=0. For each H/a, three cases with different substrate thicknesses are studied: a/h = 0.9, 2.5 and 10.0.

4.2.3 Discussions

We have identified three different delamination modes under shear separation: i) Mode-I crack propagation, ii) Mode-II crack propagation, and iii) interface cavitation. Which mode would occur depends on the stress state in the elastic substrate developed during delamination, which is governed by essentially two parameters: *H*/*a* representing height of the applied shear force and *a*/*h* representing the substrate thickness. Using the FE data, we plot a phase diagram of the delamination modes in Fig.13. Briefly, either the Mode-I crack propagation mode (circular symbols) or interface cavitation mode (triangular symbols) would occur at large *H*/*a* where rotation of the rigid punch results in a region with concentrated normal traction near the left edge of the contact area. Delamination tends to occur through interface cavitation for very thin substrates (i.e., large *a*/*h*), and through Mode-I crack propagation for thicker substrates. On the other hand, the Mode-II crack propagation (square symbols) occurs when the punch rotation is suppressed by the small *H*/*a*.

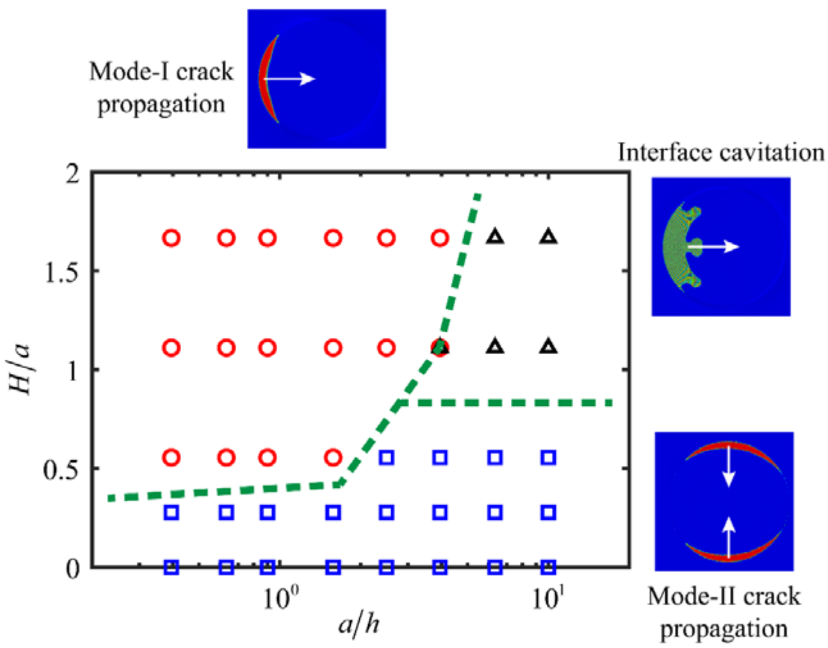

Figure 13 Phase diagram of the three delamination modes with respect to *H/a* and *a/h*.

The effect of punch rotation on the pull-off force observed in the 3D FE model is qualitatively similar to that in the 2D plane strain model. To illustrate this point, recall the analytical solution of normalized pull-off force for the 2D model given in Eq.(2.27). By setting α =0, we obtain

$$\bar{F}_c = \frac{1}{\sqrt{4(H/a)^2+1}} \quad . \tag{4.7}$$

Note that this normalized pull-off force of the 2D model is equivalent to that of the 3D model (see Eq.(4.2)): both definitions use the corresponding normal pull-off force for infinitely thick substrates as the reference. As shown in Fig.14, Eq.(4.7) predicts that $\bar{F}_c$ scales with $(H/a)^{-1}$ when H/a >>1. This trend is consistent with the 3D case with thick substrate (a/h<<1) which is obtained by extrapolating the empirical formulas in Eqs.(4.4)-(4.6) to the limit of $a/h \to 0$, and is illustrated in Fig.14 using asterisk symbols. Indeed, the quantitative agreement between the 2D solution and 3D data for thick substrate (a/h <<1) is remarkable. This suggests that Eq.(4.7) can be used as a quantitative guide for estimating the effect of the height H on pull-off force for thick substrates. Interestingly, the scaling relation that the pull-off force $F_c \sim (H/a)^{-1}$ when H/a >>1 was also observed in the experimental data of Chaudhury and Kim[20], even though our 2D model assumes an elastic half space (a/h<<1) while the experimental data[20] were for thin substrates (a/h >>1).

The FE data for a case of thin substrate (a/h =3.95) are also plotted in Fig.14 for comparison. Interestingly, a non-monotonic dependence of the pull-off force on H/a is observed, which is due to the transition of delamination modes as H/a is increased. As shown in Fig.13, when a/h=3.95 and H/a < ~ 0.56, the dominating delamination mode is Mode-II crack propagation. With this mode, increasing H/a can cause slight rotation of the punch which may reduce the energy release rate associated with the Mode-II interface crack and hence lead to an increase in pull-off force. However, when H/a > ~ 0.56, the dominating delamination mode becomes Mode-I crack propagation where increasing H/a can reduce the pull-off force by promoting punch rotation and thus enhancing local Mode-I energy release rate at the left edge of the contact area.

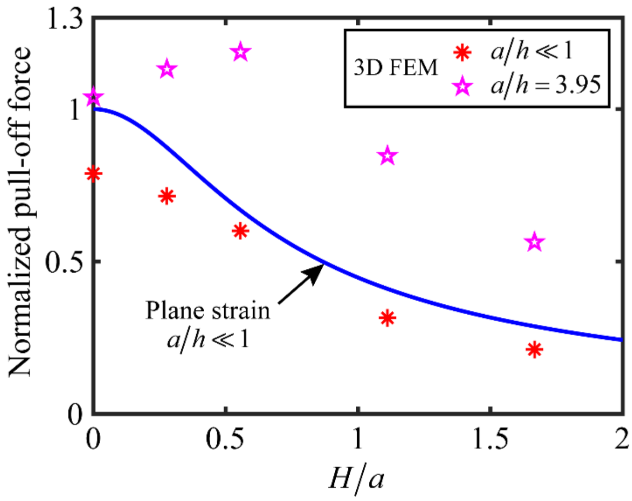

Figure 14 Normalized pull-off force versus *H*/*a* given by the 2D plane strain model (solid line) and 3D model for *a*/*h* <<1 (asterisks) and *a*/*h* = 3.95 (stars).

4.3 Combined shear and normal forces: effect of loading angle

In this section, we consider the scenario where the punch is subjected to combined shear and normal forces, with the resultant force pointing along an angle α above the horizontal direction (see Fig.5a). Our focus is on how the loading angle α affects the pull-off force, and therefore we fix *H*/*a* =1.11 but vary the substrate thickness (i.e., *a*/*h*). The FE data of pull-off forces are shown in Fig.15, which shows that the pull-off force increases as the loading angle increases from 0 to π/2. In this set of simulations, we only observe two delamination modes: Mode-I crack propagation (circular symbols) and interface cavitation (triangular symbols), similar to the case of shear separation with large *H*/*a* (see Fig.9 and 10). In addition, the pull-off force resulting from the Mode-I crack propagation mode can also be well fitted by Eq.(4.4) through shifting the normal pull-off force curve, and the coefficients C_1 to C_5 for different angles α are summarized in Table 2.

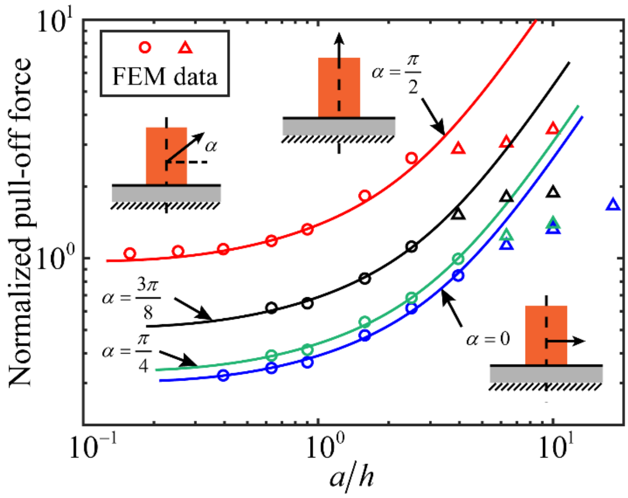

Figure 15 Normalized pull-off force versus *a/h* with different loading angles α and H/a =1.11. The symbols (circles: Mode-I crack propagation; triangles: interface cavitation) represent our FE results. The solid lines are obtained by fitting Eq.(4.4) to the FE data with the corresponding coefficients given in Table 2.

Table 2 Coefficients for the empirical formula Eq.(4.4) of pull-off force under combined normal and shear forces with H/a =1.11 and different angles α.

α	**Valid for**	C_1	C_2	C_3	C_4	C_5
0	a/h <3.95	2.0892	1.6472	0.1202	4.3562	0.3117
π/8	a/h<3.95	2.0224	1.9084	0.1869	5.0469	0.4847
π/4	a/h<3.95	2.3198	1.7146	0.1355	4.5344	0.3515
3π/8	a/h<2.5	3.5041	1.8739	0.1770	4.9558	0.4589
π/2	a/h<2.5	$\frac{8}{3}\sqrt{2\pi}$	2.2002	0.2864	5.8186	0.7427

Interestingly, the FE results suggest that the pull-off force is insensitive to the loading angle when α is below π/4. When α exceeds π/4, the pull-off force rapidly increases with α and approaches the limit of normal separation. To illustrate this behavior, in Fig.16 we plot the dependence of normalized pull-off force $\overline{F}_c$ on the loading angle α. For the 3D model, we include two cases: i) thick substrate (a/h<<1) by extrapolating Eq.(4.4) with the coefficients given in Table 2, and ii) a case representing thin substrate (a/h =3.95). The qualitatively trend of how $\bar{F}_c$ on the loading angle α for both thick and thin substrates agrees with that of the 2D model predicted by the analytical solution Eq.(2.27). Again, this agreement shows that Eq.(2.27) derived from the 2D model can be used for estimating the effect of loading angle in the 3D case with cylindrical punch.

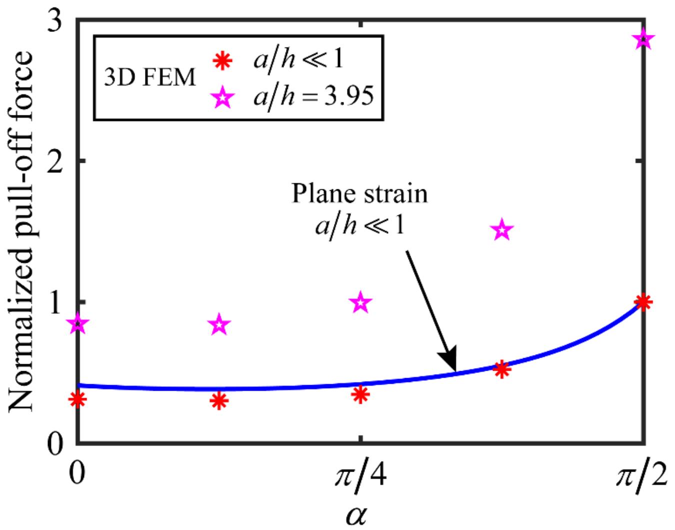

Figure 16 Normalized pull-off force versus the loading angle for H/a =1.11 given by the 2D plane strain model (solid line) and 3D model for a/h << 1 (asterisks) and a/h = 3.95 (stars).

5. Summary and Conclusions

We presented a theoretical and computational study on the delamination of a rigid punch from an elastic substrate under normal and shear forces. We first studied a 2D plane strain model to gain theoretical insights and then developed a 3D FE model to simulate the complex 3D mechanics involved in the delamination process. From the 2D model, we derived an analytical solution for the pull-off force using a fracture mechanics approach. This solution, although based on the assumption of an elastic half-space substrate, was found to capture the quantitative trend of how pull-off force depend on the loading position H and loading angle α exhibited in the 3D FE results with thick substrates. Both the 2D analytical model and 3D FE model show that given the same properties of substrate (i.e., E and h) and interface (i.e., W_{ad} and a), normal separation requires the largest pull-off force. The main physical mechanism behind the lower pull-off force for shear or angled separation is the uneven normal traction due to the punch rotation, which causes delamination to initiate locally near an edge of the contact area as opposed to along the entire periphery during normal separation. For shear separation, we identified three delamination modes: Mode-I crack propagation, Mode-II crack propagation and interface cavitation. Empirical formulas were obtained for pull-off forces governed by the first two modes.

Our results have practical implications for the design of fouling release or anti-icing coatings. Since the delamination force in reality may include both normal and shear components, the empirical formulas in our work can provide more accurate estimate of the pull-off force, thereby facilitating the development of more efficient release methods. For example, it is advantageous to apply shear force during delamination which can greatly reduce the pull-off force. In addition, a common principle of the delamination modes with low pull-off force is to promote the initiation of local delamination, either through interface cavitation or the introduction of uneven tractions on the contacting interface. This principle is consistent with the approach of interface crack initiator recently exploited to improve the release performance of anti-icing coatings[44].

There are several limitations in this study that could be addressed in future work. First, we assumed infinitesimal deformation and linear elasticity for the substrate to enable analytical solution for the 2D model and to reduce independent parameters for the 3D FE model. Although this is a relevant assumption for many coating applications, large deformation may occur for strong adhesion and soft substrate. In this case, nonlinearity associated with large deformation may further complicate the delamination mechanics[45,46]. This question remains to be answered. Second, we have not discussed in detail the pull-off force governed by the interface cavitation mode. The FE simulation of interface cavitation would require an extensive imperfection sensitivity study to validate the FE results, but this will be necessary if thin coatings are encountered (i.e., $a/h \gg 1$). Third, in practice the rigid object to be detached from the elastic substrate possesses more complex structure[21,47]. For example, barnacles, a common marine fouling organism, are known to have a hollow shell structure rather than a solid punch. The substrate may not be uniform either: mechanical heterogeneities may be deliberately incorporated to promote local delamination on the interface. How these complex structures affect the delamination process, especially under shear or angled separation, remains an open question and requires further studies.

Acknowledgements

X.H.S. and H.A.W. acknowledge support from the Strategic Priority Research Program of the Chinese Academy of Sciences (XDB22040402) and the National Natural Science Foundation of China (11525211, 11872036). L.Y., M.E.R. and R.L. acknowledge National Science Foundation for funding this work through grant CMMI-1636203. This work used the Extreme Science and Engineering Discovery Environment (XSEDE) through allocation MSS160030, which is supported by National Science Foundation grant number ACI-1548562.

Appendix 1 Finite element model: effect of mesh size and cohesive parameter.

In our simulations, the cohesive zone models and mesh designs will significantly impact the FE results of pull-off forces. To validate our computational model, we perform sensitivity studies regarding the cohesive zone model and mesh size as detailed below.

Two representative traction-separation laws for the cohesive zone model tested in the simulation are shown in Fig.17b. In both cases, the following adhesion energy W_{ad} is adopted to ensure a small deformation of the substrate:

$$\frac{W_{ad}}{\mu a} = 0.005\,, \tag{A1.1}$$

where μ=E/3 denotes the shear modulus of the substrate. The maximum separation δ_f values, which are much smaller than the contact radius a, i.e. δ_f/a =0.01 and 0.02, are chosen such that the detailed shape of the traction-separation curve will have negligible effects on the interface adhesive behavior[38]. For each traction-separation law, the mesh convergence test is performed to obtain a mesh-independent pull-off force, as shown in Fig.17a.

We focus on the normal separation case with a moderate substrate thickness (a/h=0.9) and use the numerical solution for the pull-off force by Yang and Li[17] shown in Fig.17a as a benchmark. The FE data for pull-off forces with two traction-separation laws are plotted against the element numbers, as shown in Fig.17a. Note that the forces are normalized to the normal pull-off force F_{c0} for an elastic half-space (a/h=0) and the dashed line represents the solution of Yang and Li[17]. As can be seen in Fig.17a, the pull-off forces for both traction-separation laws get converged as the mesh is refined. However, the pull-off force for δ_f/a =0.01 has achieved a better agreement with the solution by Yang and Li[17]. This is expected since an interface in linear fracture mechanics can be theoretically characterized by a traction-separation law in the Dirac-function form, implying that a smaller δ_f/a can result in a more accurate simulation of the interface fracture behavior. Another implication by Fig.17a is that a smaller δ_f/a will require a more refined mesh design to achieve the mesh-independent results. Interestingly, when the element size at the edge of the contact region is exactly equal to δ_f, mesh convergence of the pull-off force is achieved. This means we cannot infinitely reduce δ_f/a considering the computational costs for reliable results. As a result, to balance computational cost and numerical accuracy, we choose the interface parameter of δ_f/a=0.01 and the mesh design of 264000 elements (see Fig.17d) to perform the delamination simulations in the present work.

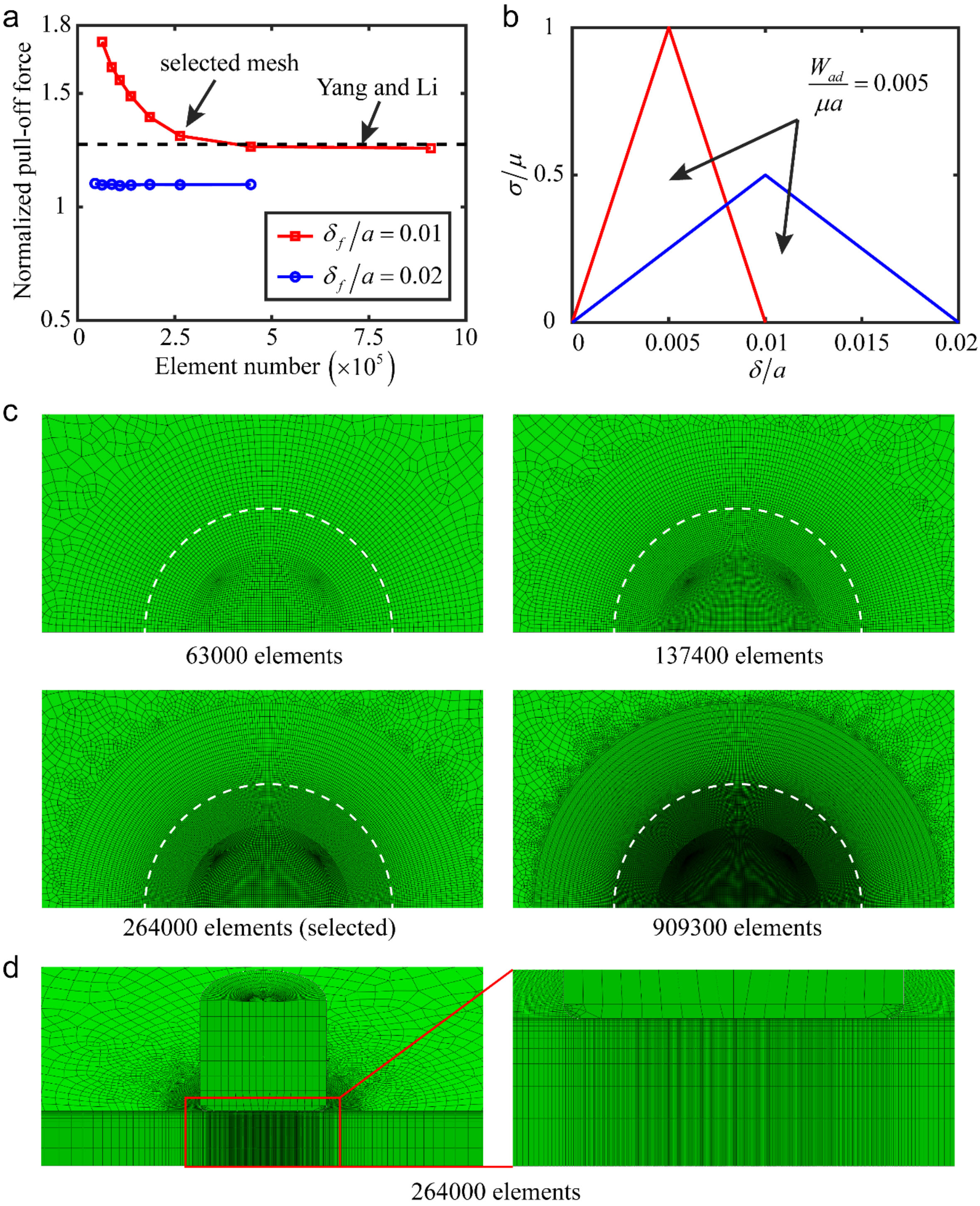

Figure 17 The mesh convergence tests with two cohesive zone models. (a) Normalized pull-off force versus element numbers under normal separation for the case of a/h=0.9 with two traction-separation laws. The corresponding numerical result by Yang and Li[17], shown in dashed line, is used as a benchmark. (b) Two representative traction-separation curves with the same adhesion energy ($W_{ad}/(\mu a)$=0.005) but different δ_f/a values (red: 0.01; blue: 0.02), where $\mu=E/3$ denotes the substrate shear modulus. (c) Several examples of the mesh designs of the contact surface used in the simulation. The white dashed line depicts the edge of contacting

region. (d) Selected mesh design of the lateral cross-section. The inset shows a magnified view of the mesh.

References

1. Schultz, M. P. Effects of coating roughness and biofouling on ship resistance and powering. *Biofouling* **23,** 331–341 (2007).
2. Piola, R. F., Dafforn, K. A. & Johnston, E. L. The influence of antifouling practices on marine invasions. *Biofouling* **25,** 633–644 (2009).
3. Evans, S. ., Birchenough, A. . & Brancato, M. . The TBT Ban: Out of the Frying Pan into the Fire? *Mar. Pollut. Bull.* **40,** 204–211 (2000).
4. Voulvoulis, N., Scrimshaw, M. D. & Lester, J. N. Alternative antifouling biocides. *Appl. Organomet. Chem.* **13,** 135–143 (1999).
5. Ellis, D. V & Agan Pattisina, L. Widespread neogastropod imposex: A biological indicator of global TBT contamination? *Mar. Pollut. Bull.* **21,** 248–253 (1990).
6. Lejars, M., Margaillan, A. & Bressy, C. Fouling Release Coatings: A Nontoxic Alternative to Biocidal Antifouling Coatings. *Chem. Rev.* **112,** 4347–4390 (2012).
7. Krishnan, S., Weinman, C. J. & Ober, C. K. Advances in polymers for anti-biofouling surfaces. *J. Mater. Chem.* **18,** 3405 (2008).
8. Salta, M. *et al.* Designing biomimetic antifouling surfaces. *Philos. Trans. A. Math. Phys. Eng. Sci.* **368,** 4729–54 (2010).
9. Grozea, C. M. & Walker, G. C. Approaches in designing non-toxic polymer surfaces to deter marine biofouling. *Soft Matter* **5,** 4088 (2009).
10. Brady, R. F. Clean hulls without poisons: Devising and testing nontoxic marine coatings. *J. Coatings Technol.* **72,** 45–56 (2000).
11. Zhuo, Y. *et al.* Enhancing the Mechanical Durability of Icephobic Surfaces by Introducing Autonomous Self-Healing Function. *ACS Appl. Mater. Interfaces* **10,** 11972–11978 (2018).

12. Wang, C., Fuller, T., Zhang, W. & Wynne, K. J. Thickness Dependence of Ice Removal Stress for a Polydimethylsiloxane Nanocomposite: Sylgard 184. *Langmuir* **30,** 12819–12826 (2014).

13. Beemer, D. L., Wang, W. & Kota, A. K. Durable gels with ultra-low adhesion to ice. *J. Mater. Chem. A* **4,** 18253–18258 (2016).

14. Golovin, K. *et al.* Designing durable icephobic surfaces. *Sci. Adv.* **2,** e1501496–e1501496 (2016).

15. Kendall, K. The adhesion and surface energy of elastic solids. *J. Phys. D. Appl. Phys.* **4,** 320 (1971).

16. Lin, Y. Y., Hui, C. Y. & Conway, H. D. Detailed elastic analysis of the flat punch (tack) test for pressure-sensitive adhesives. *J. Polym. Sci. Part B Polym. Phys.* **38,** 2769–2784 (2000).

17. Yang, F. & Li, J. C. M. Adhesion of a Rigid Punch to an Incompressible Elastic Film. (2001). doi:10.1021/LA010409H

18. Singer, I. L., Kohl, J. G. & Patterson, M. Mechanical aspects of silicone coatings for hard foulant control. *Biofouling* **16,** 301–309 (2000).

19. Brady, R. F. & Singer, I. L. Mechanical factors favoring release from fouling release coatings. *Biofouling* **15,** 73–81 (2000).

20. Chaudhury, M. K. & Kim, K. H. Shear-induced adhesive failure of a rigid slab in contact with a thin confined film. *Eur. Phys. J. E* **23,** 175–183 (2007).

21. Chung, J. Y. & Chaudhury, M. K. Soft and Hard Adhesion. *J. Adhes.* **81,** 1119–1145 (2005).

22. Kohl, J. G. & Singer, I. L. Pull-off behavior of epoxy bonded to silicone duplex coatings. *Prog. Org. Coatings* **36,** 15–20 (1999).

23. Crosby, A. J., Shull, K. R., Lakrout, H. & Creton, C. Deformation and failure modes of

adhesively bonded elastic layers. *J. Appl. Phys.* **88,** 2956 (2000).

24. Webber, R. E., Shull, K. R., Roos, A. & Creton, C. Effects of geometric confinement on the adhesive debonding of soft elastic solids. *Phys. Rev. E - Stat. Physics, Plasmas, Fluids, Relat. Interdiscip. Top.* **68,** 11 (2003).

25. Lakrout, H., Sergot, P. & Creton, C. Direct observation of cavitation and fibrillation in a probe tack experiment on model acrylic pressure-sensitive-adhesives. *J. Adhes.* **69,** 307–359 (1999).

26. Creton, C. & Lakrout, H. Micromechanics of Flat-Probe Adhesion Tests of Soft Viscoelastic Polymer Films. *J. Polym. Sci. Part B Polym. Phys.* **38,** 965–979 (2000).

27. Chaudhury, M. K., Chakrabarti, A. & Ghatak, A. Adhesion-induced instabilities and pattern formation in thin films of elastomers and gels. *Eur. Phys. J. E* **38,** 82 (2015).

28. Schultz, M. P., Kavanagh, C. J. & Swain, G. W. Hydrodynamic forces on barnacles: Implications on detachment from fouling-release surfaces. *Biofouling* **13,** 323–335 (1999).

29. Swain, G. W., Griffith, J. R., Bultman, J. D. & Vincent, H. L. The use of barnacle adhesion measurements for the field evaluation of non-toxic foul release surfaces. *Biofouling* **6,** 105–114 (1992).

30. Swain, G. W. & Schultz, M. P. The testing and evaluation of non-toxic antifouling coatings. *Biofouling* **10,** 187–197 (1996).

31. Shull, K. R. & Crosby, A. J. Axisymmetric Adhesion Tests of Pressure Sensitive Adhesives. *J. Eng. Mater. Technol.* **119,** 211 (1997).

32. Ganghoffer, J. F. & Gent, A. N. Adhesion of a Rigid Punch to a Thin Elastic Layer. *J. Adhes.* **48,** 75–84 (1995).

33. Hensel, R., McMeeking, R. M. & Kossa, A. Adhesion of a rigid punch to a confined elastic layer revisited. *J. Adhes.* 1–20 (2017). doi:10.1080/00218464.2017.1381603

34. Beemer, D. L., Wang, W. & Kota, A. K. Durable gels with ultra-low adhesion to ice. *J. Mater. Chem. A* **4,** 18253–18258 (2016).

35. Johnson, K. L. *Contact Mechanics*. (Cambridge University Press, 1985). doi:10.1017/CBO9781139171731

36. Adams, G. G. Frictional slip of a rigid punch on an elastic half-plane. *Proc. R. Soc. A Math. Phys. Eng. Sci.* **472,** 20160352 (2016).

37. Rice, J. R. Elastic Fracture Mechanics Concepts for Interfacial Cracks. *J. Appl. Mech.* **55,** 98 (1988).

38. Hui, C. Y., Ruina, A., Long, R. & Jagota, A. Cohesive Zone Models and Fracture. *J. Adhes.* **87,** 1–52 (2011).

39. Shull, K. R., Flanigan, C. M. & Crosby, A. J. Fingering instabilities of confined elastic layers in tension. *Phys. Rev. Lett.* **84,** 3057–3060 (2000).

40. Yang, F. Indentation of an incompressible elastic film. *Mech. Mater.* **30,** 275–286 (1998).

41. Chadwick, R. S. Axisymmetric Indentation of a Thin Incompressible Elastic Layer. *SIAM J. Appl. Math.* **62,** 1520–1530 (2002).

42. Long, R., Hui, C.-Y., Kim, S. & Sitti, M. Modeling the soft backing layer thickness effect on adhesion of elastic microfiber arrays. *J. Appl. Phys.* **104,** 044301 (2008).

43. Chung, J. Y., Kim, K. H., Chaudhury, M. K., Sarkar, J. & Sharma, A. Confinement-induced instability and adhesive failure between dissimilar thin elastic films. *Eur. Phys. J. E* **20,** 47–53 (2006).

44. He, Z., Xiao, S., Gao, H., He, J. & Zhang, Z. Multiscale crack initiator promoted super-low ice adhesion surfaces. *Soft Matter* **13,** 6562–6568 (2017).

45. Lin, S. *et al.* Fringe instability in constrained soft elastic layers. *Soft Matter* **12,** 8899–8906 (2016).

46. Lin, S., Mao, Y., Radovitzky, R. & Zhao, X. Instabilities in confined elastic layers under tension: Fringe, fingering and cavitation. *J. Mech. Phys. Solids* **106,** 229–256 (2017).

47. Hui, C.-Y., Long, R., Wahl, K. J. & Everett, R. K. Barnacles resist removal by crack trapping. *J. R. Soc. Interface* **8,** 868–79 (2011).